Author/s:
Warner, T;Rinaudo, M;Xu, Y;Han, J;Ashokan, A;Kirkwood, N;Widmer-Cooper, A;Smith, TA;Ghiggino, KP;Rosengarten, G

Title:
Effect of luminescent nanocrystal alignment on fluorescence anisotropy and light guiding in polymer films

Date:
2025-02

Citation:
Warner, T., Rinaudo, M., Xu, Y., Han, J., Ashokan, A., Kirkwood, N., Widmer-Cooper, A., Smith, T. A., Ghiggino, K. P. & Rosengarten, G. (2025). Effect of luminescent nanocrystal alignment on fluorescence anisotropy and light guiding in polymer films. Optical Materials, 159, https://doi.org/10.1016/j.optmat.2024.116606.

Persistent Link:
https://hdl.handle.net/11343/354918

Effect of luminescent nanocrystal alignment on fluorescence anisotropy and light guiding in polymer films

Timothy Warner, Michael Rinaudo, Yang Xu, Jiho Han, Arun Ashokan, Nicholas Kirkwood, Asaph Widmer-Cooper, Trevor A. Smith, Kenneth P. Ghiggino, and Gary Rosengarten

Optical Materials
Volume 159, February 2025, 116606

https://doi.org/10.1016/j.optmat.2024.116606

Effect of luminescent nanocrystal alignment on fluorescence anisotropy and light guiding in polymer films

Timothy Warner[a,b,1], Michael Rinaudo[c], Yang Xu[b], Jiho Han[b], Arun Ashokan[b], Nicholas Kirkwood[b], Asaph Widmer-Cooper[c,d], Trevor A. Smith[b], Kenneth P. Ghiggino[b*], and Gary Rosengarten[a]

[a] *School of Engineering, RMIT University, 115 Queensberry St, Carlton, 3053, VIC, Australia*

[b] *ARC Centre of Excellence in Exciton Science, School of Chemistry, The University of Melbourne, Parkville, 3010, VIC, Australia*

[c] *ARC Centre of Excellence in Exciton Science, School of Chemistry, University of Sydney, Sydney, New South Wales 2006, Australia*

[d] *The University of Sydney Nano Institute, University of Sydney, Sydney, New South Wales 2006, Australia*

**Author for correspondence*

Abstract

Elongated semiconductor nanocrystals with oriented transition dipoles, such as nanorods (NRs) and elongated nanoplatelets (NPLs), can exhibit emission anisotropy when confined in thin films. In this work, we report the effect of nanocrystal alignment on thin polymer film optical properties including absorbance, fluorescence polarisation and light guiding. We find that changes in absorbance after stretching films containing elongated nanocrystals are associated with changes in nanocrystal alignment. Stretching the NPL films induces fluorescence anisotropy, which follows an exponential trend that can be approximated as linear within a moderate range of true strain values. This empirical relationship provides a means to monitor strain in polymers undergoing deformation. The light guiding properties of polymer films containing luminescent nanocrystals are also investigated by applying experimental and Monte Carlo simulation methodologies developed for the luminescent solar concentrator field. We show that drop cast polymer films containing spherical quantum dots, with isotropic fluorescence, more effectively guide light to the film edges compared with elongated nanocrystals. The elongated nanocrystals are aligned in the film plane by both stretching and drop casting processes, resulting in increased fluorescence emission from the film faces due to escape cone losses.

Keywords: Nanocrystal alignment, fluorescence anisotropy, light guide, nanorod, nanoplatelet, true strain, luminescent solar concentrator

1. Introduction

There is an ever-expanding use of luminescent nanocrystals in modern technologies. Their applications include illumination and display technologies, photovoltaics, fluorescent biomarkers, photodetectors and

[1] *Present address: Chemical Engineering, McMaster University, 1280 Main St W, Hamilton, L8S 4L8, ON, Canada*

luminescent solar concentrators (LSCs) [1-6]. One of the key advantages of luminescent semiconductor nanocrystals, such as quantum dots (QDs), nanorods (NRs) and nanoplatelets (NPLs), is that they have tuneable optical, chemical and electrical properties based on their chemical composition, size and shape [7]. The small size of these particles results in the confinement of electron motion giving control over the electronic structure based on the size and shape of the nanocrystal [7]. The confinement can occur in three dimensions, such as with QDs, or it can be in only one or two dimensions, such as with NPLs and NRs respectively [8]. For the latter cases there exists, in general, a major transition dipole along the least confined direction (the long axis), which results in directional emission perpendicular to the long axis [8]. In addition, the photoluminescence will tend to be polarised parallel to the long axis for NRs and elongated NPLs in most cases [8, 9]. Recently, there has also been the development of more complex nanocrystal morphologies such as nanotetrapods (NTPs), semiconductor nanocrystals with four arms extending from a core, and hierarchical flower-like structures [10, 11]. Polarised fluorescence is observed from NTPs due to differences in arm diameter [12]. Additionally, NTPs with long arms exhibit large Stokes shifts, effectively eliminating reabsorption in thin polymer films, which is beneficial for LSC applications [10]. For the purposes of this study, we focus on NRs and elongated NPLs and refer to them as elongated nanocrystals.

When elongated nanocrystals are aligned in polymer films they exhibit fluorescence polarised parallel to the alignment direction of the nanocrystals, shown in Figure 1 (a) and (b) [1]. Alignment of elongated nanocrystals within polymer matrices has been achieved using various methods. Extrusion and injection moulding of polymers containing gold nanorods has been shown to be a method to align nanocrystals [13]. Another method investigated to align elongated nanoparticles in a polymer film is stretching a film which contains initially unaligned particles [14, 15]. The requirement to first disperse the nanoparticles in the matrix before alignment is common to both alignment methods [13-15]. Alignment of nanorods in a polymer matrix using electric fields has been attempted, however alignment was not observed [16].

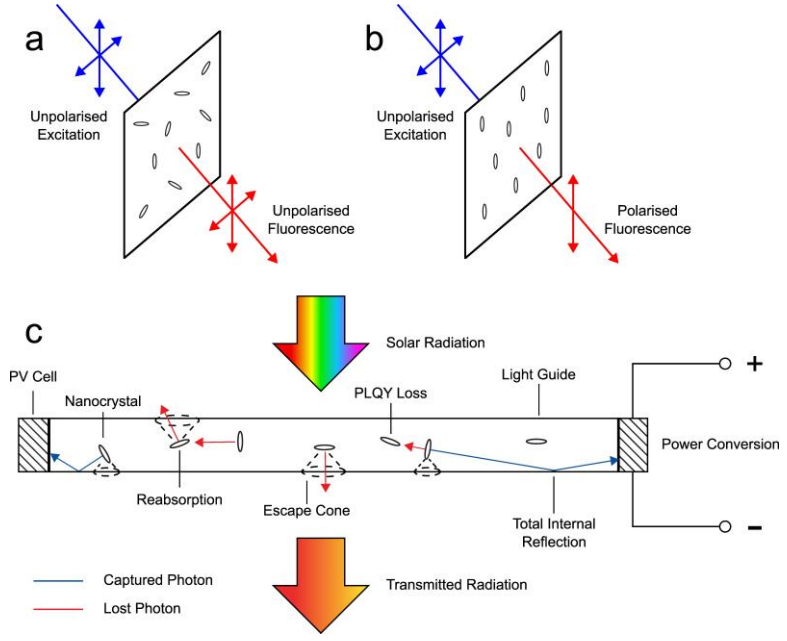

Figure 1. Demonstration of fluorescence polarisation by (a) unaligned and (b) aligned luminescent nanocrystals. (c) Schematic representation of anisotropic nanocrystals, such as nanorods or elongated nanoplatelets, randomly oriented in a light guide with associated light loss mechanisms shown. The effects of particle orientation on emission processes and escape cone losses are also shown.

One method to assess the fluorescence polarisation properties of films is by measuring the fluorescence

anisotropy. Fluorescence anisotropy measurements are conducted by exposing the film to a polarised excitation light source then measuring the fluorescence polarised parallel and perpendicular to the polarisation of the excitation. Details of the measurement and calculation of fluorescence anisotropy are included in Experimental Section 2.5 [17]. Time-resolved fluorescence anisotropy is often utilised in studies of molecular motion or Förster resonance energy transfer (FRET) between luminophores [17]. However, for the present study, steady state fluorescence anisotropy measurements have been applied as molecular rotation is supressed for nanocrystals in solid polymer films and the nanocrystal concentrations are low, so FRET is not possible.

Fluorescence anisotropy (r) has previously been used to assess the stress and strain of polymer films containing alignable fluorescent dyes [18-22]. Deformation during biaxial stretching of polymer films can be monitored by measuring the fluorescence polarisation in the two stretching directions [19]. Similarly, the uniaxial deformation of polymer films has been measured by utilising fluorescence anisotropy measurements of fluorescent dyes in polymer matrices [18, 21]. It was shown quantitatively that fluorescence anisotropy increases with extension, otherwise known as engineering strain, defined as the ratio of the change in specimen length to the initial specimen length [21]. For that study we have analysed the residuals of the linear model applied to the data and found that it better follows a curved relationship. A linear relationship between fluorescence anisotropy and true stress has also been claimed [18]. True stress is the force across the instantaneous specimen cross-sectional area as it changes during deformation. It must be considered that fluorescence anisotropy has a possible range of $-0.5 < r < 1$, therefore the linear relationship demonstrated was likely a linear portion of a non-linear relationship [18, 19, 23]. The relationship between fluorescence anisotropy and true strain, the instantaneous change in specimen length, has to our knowledge not been investigated previously. Additionally, we are not aware of reports using fluorescence anisotropy for monitoring the strain in polymer films utilising fluorescent nanocrystals.

Light guides are devices that utilise total internal reflection (TIR) to transport light [24]. To study the light guiding properties of fluorescent films, we are using methodologies and terminology developed in the LSC field [25]. LSCs typically consist of a fluorescent material embedded in, or coated on, a transparent medium such as a sheet of glass or polymer [26]. A wide range of fluorescent materials have been investigated including fluorescent dyes, rare earth ions, QDs and other inorganic semiconductor materials [5, 27, 28]. The operating principle is that a high proportion of the fluorescence is trapped within the higher refractive index transparent medium through TIR and is "light guided" to the edge of the sheet where the light can be collected by photovoltaic (PV) cells to generate electrical power, as shown in Figure 1 (c) [26, 29].

A range of factors limit the light guiding efficiency of films including transmission losses, photoluminescence quantum yield (PLQY) losses, escape cone losses and reabsorption losses that compound PLQY and escape cone losses [25, 30]. The transmission and PLQY losses are highly dependent on the properties of the fluorescent material used, whereas the escape cone losses are dependent on the refractive index of the transparent medium as well as the directionality of the emission. Films utilising nanoparticles can suffer an additional scattering loss mechanism if aggregation of the nanoparticles occurs [31, 32]. Ensuring good compatibility between the polymer matrix and the nanoparticles can significantly reduce aggregation and scattering in the waveguide [30, 32, 33]. Previous studies have shown that aligning organic dyes so that their emission is in the plane of the light guide reduces the escape cone losses and improves the internal photon efficiency (η_{int}) (defined as the number of photons emitted from the waveguide edges relative to the number of photons absorbed, also commonly referred to as optical quantum efficiency or OQE) [25, 34]. Additionally, modelling has shown that alignment of fluorescent semiconductor nanorods perpendicular to the film face should also reduce escape cone losses [35, 36]. However, there is minimal experimental data related to alignment of semiconductor nanoparticles in polymer matrices for LSC applications [37, 38]. A recent study showed that stretching polymer films containing nanorods resulted in nanorods aligned in the stretching direction, however the conclusion that this orientation is the optimal angle for reducing escape cone losses is not supported by previous modelling results [35, 39].

In the present study, we report the absorption and emission properties of CdSe/CdS core-shell QDs and NRs and CdSe/CdZnS core-shell NPLs in poly(vinyl butyral) (PVB) matrices. We examine the alignment of nanocrystals in drop cast and stretched films, and measure the fluorescence anisotropy of the films, to understand how alignment affects optical properties. Subsequently we study the relationship between true strain and fluorescence anisotropy for films containing NPLs. Finally, we examine the effects of aligning the NRs and NPLs on the light guiding efficiency. Utilising methodologies related to LSCs, we determine the light guiding efficiencies of films containing fluorescent nanocrystals. The light guiding experiments are supported by ray-tracing simulations based on theory and simplified assumptions about the nanocrystal orientations in the films. This investigation establishes a true strain - fluorescence anisotropy relationship using embedded NPLs that may find general application. In addition, an examination of light guiding efficiencies of the stretched films provides experimental verification of modelling of aligned nanocrystals embedded in light guides.

2. Experimental

2.1. Nanoparticle Synthesis

A variety of CdSe/CdS semiconductor nanocrystals were synthesised using established methods from the literature. The CdSe/CdS core shell quantum dots (QDs) were made using a hot-injection synthesis method [40]. The CdSe/CdS nanorods (NRs) were made in a two-step reaction where an elongated shell is grown around a spherical core to form dot-in-rod nanoparticles [41]. The nanoplatelets (NPLs) were also grown in a two-step synthesis starting with CdSe NPL cores then growing a $Cd_xZn_{1-x}S$ shell around them [42, 43]. The first synthesis resulted in elongated NPLs with a long and a short axis. The thickness of the particles started as several atomic monolayers but increased after the shelling process. The absorption and emission spectra of the nanoplatelets matched the spectra for CdSe/$Cd_xZn_{1-x}S$ nanoplatelets with 4 monolayer cores reported using the same synthesis method [43], confirming successful synthesis of the nanoplatelets. The QDs and the NPLs were then suspended in hexane and the NRs were suspended in toluene. The ligands on the nanocrystals were a combination of cadmium oleate and oleylamine resulting in hydrophobic surfaces for all the nanocrystals.

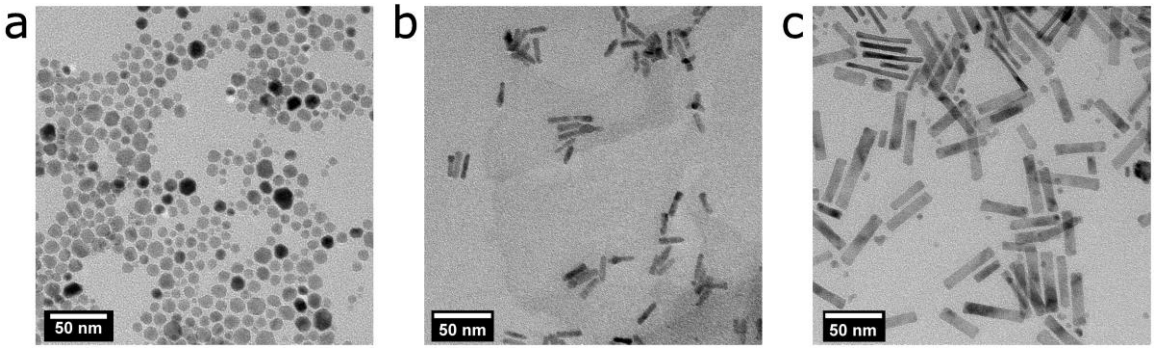

Figure 2. TEM micrographs of the fluorescent nanocrystals as cast from solution on copper supported carbon grids. The images show (a) quantum dots (QD), (b) nanorods (NR) and (c) nanoplatelets (NPL).

The size and shape of the nanocrystals are shown in Figure 2. The synthesised QD had a diameter of 10 nm ± 3 nm, the NRs had a length of 20 nm ± 3 nm and diameter of 5.1 nm ± 0.9 nm and the NPLs had a length of 40 nm ± 11 nm, width of 9 nm ± 1 nm and thickness of 4.7 nm ± 0.6 nm. The distribution of dimensions for each of these particles is presented in the Supporting Information (Figures S1-S6).

2.2. *Film Casting and Stretching*

Poly(vinyl butyral-co-vinyl alcohol-co-vinyl acetate) (PVB) was the selected polymer film substrate because it has good compatibility with the oleate and oleylamine ligands chosen in the synthesis step, allowing for good dispersion of the nanoparticles in the film samples [44]. The material properties that make PVB an effective substrate in this application are high transparency, good thermal stability and processability including solubility in a wide range of solvents. PVB (vinyl butyral 88 wt. % - 418412 Sigma-Aldrich) was dissolved in chloroform at a concentration of 100 mg/mL. The nanocrystals dispersed in hexane or toluene were dried then redispersed in chloroform. 2.4 mg of nanoparticles in chloroform were mixed with 3mL of PVB/chloroform solution then drop cast onto glass slides to cover the whole surface area to achieve a concentration of 0.8 wt %. The slides were then covered and placed in a fume hood overnight to allow the chloroform to evaporate. The slides were then placed under vacuum for a further 2 hours to remove residual chloroform. The hydrophobic butyral side groups on the PVB assisted the solubility of the nanoparticles allowing them to be dispersed within the polymer matrix [45].

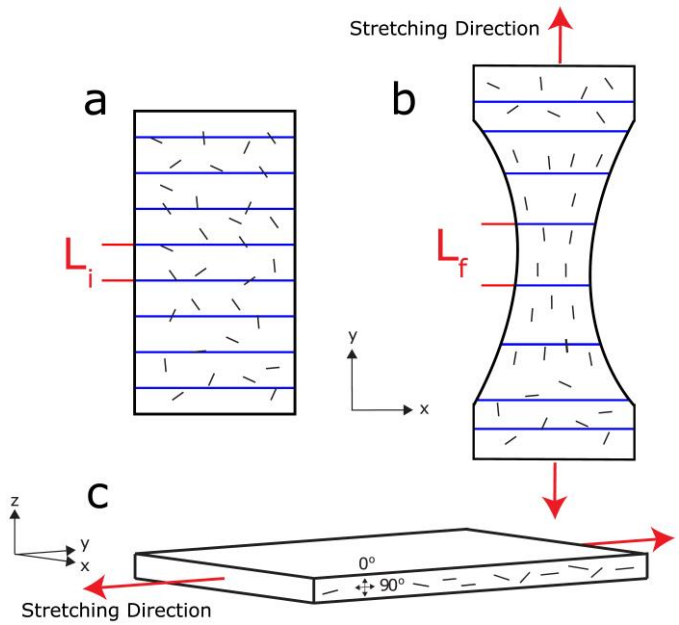

Figure 3. Schematic representation of the stretching procedure (a) the unstretched film containing nanocrystals, marked at periodic intervals (initial length = L_i) to facilitate strain measurements (b) stretched film containing nanocrystals demonstrating how the spacing between the markings change (final length = L_f) after stretching. The nanocrystals are aligned during the stretching process [1]. (c) Side view of the stretched sample defining the sample axes and demonstrating the angle relative to the z-axis referenced in the transmission electron microscopy (TEM) images and analysis.

The films were then separated from the glass slides resulting in ~100 μm thick films. Film deformation is commonly described by elongation, which is defined by the ratio of the final length (L_f) to the initial length (L_i) expressed as a percentage. The central region of the films was stretched to 400% elongation using gravity and heat, which was measured using the periodic markings on the samples shown in Figure 3 (a) and (b). A 51.5 g mass was attached to the bottom of the film and allowed to hang, which corresponded to a force of approximately 0.5 N, while heat was applied with a heat gun at the centre of the film until it stretched to 400 % elongation. While elongation is a convenient and easily understood term, a better measure of deformation is strain, specifically true strain (ε). In cases where there is a significant change in the length and cross-sectional area, as is the case with these experiments, true strain is the most representative value to describe

the deformation [46]. True strain is defined as the increase in sample length relative to the instantaneous length as opposed to engineering strain which is the increase in sample length relative to the original sample length [46]. By integrating dL/L we arrive at the mathematical description of true strain is shown in Equation 1 [46].

$$\epsilon = ln\left(\frac{L_f}{L_i}\right) \qquad \text{(Equation 1)}$$

where L_f is the final length of a film section and L_i is the initial length of the same length section.

As the deformation of the films was mediated by heat, the location of the deformation could be controlled. Resultantly, different regions of the film had different strains which could be calculated by measuring the change in the spacing of the periodic marking and applying Equation 1. For example, an area with elongation of 400% corresponds to a true strain value of 1.39. This allowed for the investigation of the effect of strain on fluorescence anisotropy for a film sample containing fluorescent NPLs.

2.3. Optical Characterisation

The absorption and fluorescence properties were characterised with an Agilent HP8453 UV-VIS spectrometer and a Horiba Jobin-Yvon Fluorolog-3 fluorimeter respectively. The absorbance of the films was measured before and after stretching but to be able to correctly compare the films the effect of the film thickness needs to be accounted for. As a result, the absorbance spectra are presented as absorbance per mm which allows determination of the effect, if any, the stretching has on the absorbance properties of the film. The fluorescence spectra were normalised for comparison purposes.

2.4. Transmission Electron Microscopy (TEM)

Transmission electron micrographs were obtained using a FEI Tecnai F20 microscope. Images of nanoparticles cast from solution were obtained to examine the morphology of the particles. Solutions of nanoparticles were dropped on carbon film supported copper grids and allowed to dry. Additionally, TEM was utilised to examine the dispersion and alignment of particles within the polymer films. This required the films to be mounted in a polymer resin block before they were sectioned by an ultra-microtome. The film samples were then cross-sectioned such that the y-z plane could be imaged, which contains both the stretch direction and thickness direction. The sections were then mounted on carbon film supported copper grids and imaged in the TEM to observe the dispersion and alignment of the nanocrystals.

2.5. Fluorescence Anisotropy

Fluorescence anisotropy measurements were undertaken to assess the effect of stretching on nanocrystal alignment. The fluorescence anisotropy measurements were performed on a scanning confocal microscope (IX71 and FV300, Olympus) to map the anisotropy at high spatial resolution. The samples are illuminated with the frequency doubled output of Ti:Sapphire laser (MIRA 900, Coherent) at 400 nm, polarised in the y-axis (stretch) direction and the fluorescence intensity polarised parallel and perpendicular to the stretch direction was measured. The fluorescence anisotropy was spatially resolved using an EMCCD camera, with fluorescence measurements being used to calculate fluorescence anisotropy on a per pixel basis. The fluorescence anisotropy (r) is given by Equation 2.

$$r = \frac{I_{VV} - G I_{VH}}{I_{VV} + 2G I_{VH}} \quad \text{(Equation 2)}$$

where I_{VV} is the fluorescence polarised parallel to the stretch direction, excited in the stretch direction, I_{VH} is the fluorescence polarised perpendicular to the stretch direction, excited in the stretch direction and G is the factor to correct for differential transmission of the orthogonal polarisations through the optical components of the instrumental set-up. The G value was calibrated on a pixel-by-pixel basis using a Rhodamine 6G reference solution. The measured G values were normally distributed with a mean value of 0.89 and standard deviation of 0.10.

2.6. PLQY and Light Guiding Efficiency

The photoluminescence quantum yield (PLQY) and internal photon efficiency (η_{int}) measurements were obtained using a Horiba F-3018 integrating sphere accessory for the fluorimeter. The internal photon efficiency was calculated using a methodology from the LSC literature that involves measuring the total emission from the film and emission from the face [30]. The internal photon efficiency can be calculated from Equation 3.

$$\eta_{int} = \eta_{PLQY} \eta_{edge} \quad \text{(Equation 3)}$$

where η_{int} is the internal photon efficiency, η_{PLQY} is the photoluminescence quantum yield of the film and η_{edge} is the edge efficiency which is defined as the ratio of edge emitted photons to the photons emitted from all film faces.

Film samples with 1 cm x 1 cm dimensions were prepared for each nanoparticle type in PVB, taken before stretching and after stretching to 400% elongation. Each sample was placed inside the integrating sphere, illuminated with 450 nm light, and their fluorescence intensity measured. The experimental values required to calculate η_{edge} are the total number of photons emitted from all sides of the film (n_{total}) illuminated inside the integrating sphere and the number of photons emitted only from the film faces (n_{faces}) that can be measured by coating the film edges with a highly absorbing black paint such that fluorescence can only leave the film via the faces. To reduce light lost due to light in the sphere hitting the black paint, a surface layer of white paint was applied on top of the black paint. The number of photons emitted from the edges (n_{out}) can then be inferred by subtracting the n_{faces} from n_{total}. The edge efficiency (η_{edge}) can then be calculated using Equation 4.

$$\eta_{edge} = \frac{n_{out}}{n_{total}} = \frac{n_{total} - n_{faces}}{n_{total}} \quad \text{(Equation 4)}$$

where n_{out} is the number of photons emitted from the edges, n_{total} is the number of photons emitted from all sides of the film and n_{faces} is the number of photons emitted from the faces.

The internal photon efficiency provides a metric for how effectively the emitted photons are reaching the edge of the film and therefore can identify the effect of nanocrystal orientation on the light guiding of the fluorescence.

2.7. Monte Carlo Ray-Tracing Simulations

Monte Carlo ray-tracing simulations were used to help interpret the experimental results. These simulations

were conducted using a modified version of an open-source ray tracing program [47]. The modifications allow for simulation of anisotropic absorption and emission by NRs in addition to isotropic luminophores such as QDs [48]. The basic steps in the simulation are as follows. First, an input photon wavelength is selected with intensity probability weighted by the AM 1.5 G solar flux spectrum. A ray normal to the film is then generated, which represents the photon, and it is either reflected, absorbed or transmitted by the film, with the likelihood of these events dependent on the non-polarised reflection of the waveguide material, the concentration and absorption spectrum of the luminophores, in this case semiconductor nanocrystals, and the thickness of the waveguide. In addition, the absorption strength of the NRs depends on alignment between the polarisation vector of the incoming photon and the axial dipole of the NRs [38]. The fate of each absorbed photon is then based on the energy either being emitted or lost, with probability depending on the PLQY of the luminophores.

For QDs, the emission was generated isotropically, with equal likelihood in all directions. For NRs, the emission is anisotropic, with the probability of emission proportional to $\sin^3(\theta)$ where θ is the angle between the emitted ray and the axis of the rod. The result of this profile is a significant preference for emission perpendicular to the axis, with 88% of rays being directed within 45 degrees of the normal of the rod axis (see Figure S17 in the Supporting Information) [49]. Depending on the direction that the ray is emitted, and the refractive index of the matrix, the photon can be lost from the faces, reabsorbed by another luminophore, or trapped by total internal reflection and emitted from the edge of the film. Compared to QDs, the anisotropic absorption and emission of the NRs results in different reabsorption properties and ray transport within the light guide.

3. Results and Discussion

3.1. Absorption and Fluorescence

The properties of fluorescent films are highly dependent on the light absorption and fluorescence properties of the fluorophore used. The absorption and emission spectra of the QDs and NRs are typical of CdSe/CdS nanocrystals with large CdS shells [31] (Figure 4 (a) and (b)). Absorption properties are predominantly derived from the CdS shell whereas fluorescence occurs due to energy transfer to the CdSe core resulting in the observed Stokes shift relative to QDs without this core shell structure [31]. The cores of both the QDs and NRs are spherical and made of CdSe and the cores are coated with large CdS shells with the main difference being that the QDs have a spherical shell whereas the NRs have an elongated shell. The absorbance and emission spectra for the NR films can be seen in Figure 4 (b). An important feature of both films is the small overlap between the absorption and fluorescence spectrum of the fluorophore leading to low reabsorption losses [31]. This large Stokes shift minimises reabsorption losses for both nanocrystals, allowing for more effective light guiding in these films. The NPLs, however, shown in Figure 4 (c), display absorption peaks that exhibit considerable spectral overlap with the fluorescence. This will increase reabsorption losses hence reduce the number of photons reaching the edge of the films.

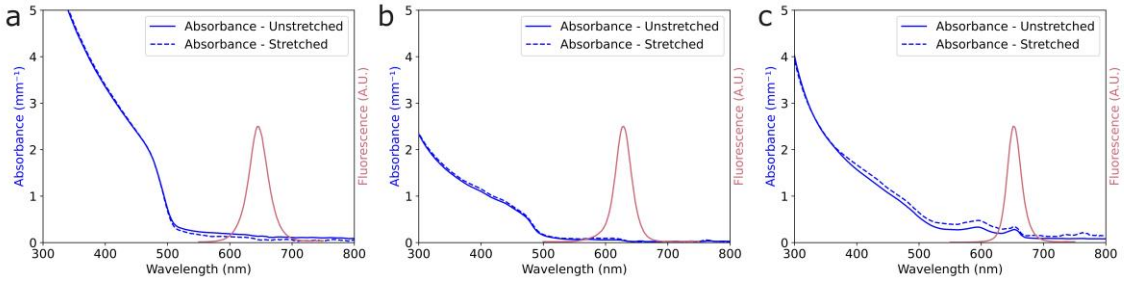

Figure 4. Absorbance and fluorescence spectra of (a) CdSe/CdS QDs (b) CdSe/CdS NRs and (c) CdSe/CdZnS NPLs. The absorbance per millimetre thickness is shown before and after stretching.

It has been shown previously that alignment of NRs parallel to the propagation direction of the incident light source reduces the absorbance of the NRs [50, 51]. It can therefore be implied that NRs oriented perpendicular to the incident light source should show an increase in absorbance relative to a random arrangement of the nanocrystal. In this way absorbance can be used to verify if the stretching has changed the orientation of the NRs relative to the z-axis, parallel to the light source and thickness direction.

The initial thicknesses of the QD, NR and NPL unstretched films were 111 μm, 129 μm and 123 μm respectively while the stretched films were 80 μm, 93 μm and 78 μm thick respectively. As expected, we do not observe any change in the thickness corrected absorbance for the QD film in Figure 4 (a). There is a very small increase in absorbance after stretching the film containing NRs in Figure 4 (b), which includes a thickness corrected absorbance increase of 0.034 mm^{-1} at 600 nm. There is a still small, but larger, increase in absorbance in the NPL film seen in Figure 4 (c) including a thickness corrected absorbance increase of 0.143 mm^{-1} at 600 nm. From this we can conclude that there is no alignment effect on the spherical QDs and that stretching has induced only a small increase in thickness corrected absorbance for the NR and NPL films implying that there were only minor changes in the angle of the particles relative to the z-axis. To investigate this result further it is necessary to observe the alignment of the nanocrystals in the y-z plane before and after stretching using TEM, see Figure 3 (c) for reference to the defined angles and planes.

3.2. Transmission Electron Microscopy

Imaging the nanocrystals inside the polymer matrix is crucial to understanding how the particles disperse in the polymer and how they are aligned relative to the z-axis. A statistically relevant selection of over 100 nanocrystals was made from TEM images of film cross-sections (y-z plane) to examine trends in the nanocrystal alignment and observe the dispersion of nanocrystals. To assist with the interpretation of the TEM images, Figure 3 shows how the axes relate to the lightguide geometry and defines the axes x, y, and z in the context of these samples. The thickness direction (z-axis) is defined as parallel to 0° and the stretching direction (y-axis) is defined as parallel to 90°.

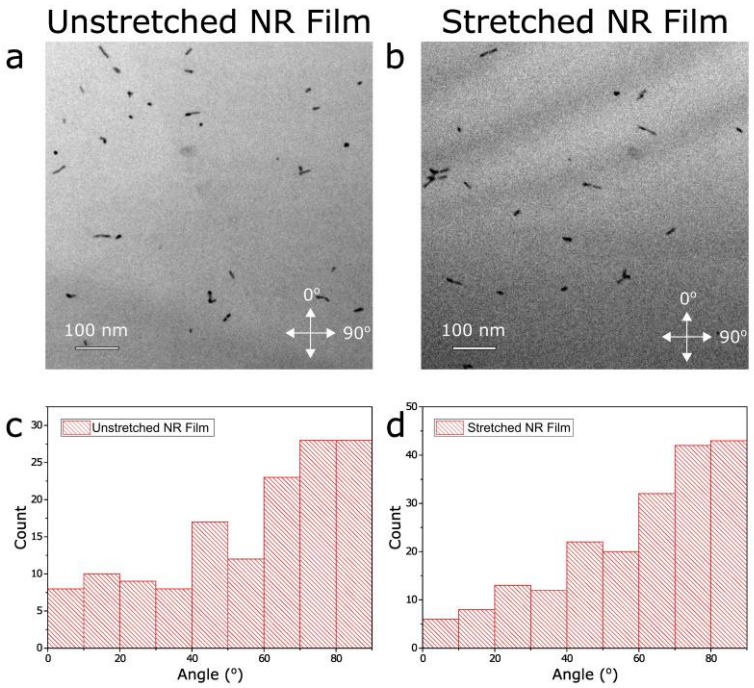

Figure 5. TEM images show representative cross-sectional areas of (a) an unstretched film

containing CdSe/CdS NRs (b) a stretched film containing CdSe/CdS NRs. The axis labelled 0° is the thickness direction (z-axis) of the films whereas 90° is the direction which will be stretched (y-axis) for (a) and the stretch direction (y-axis) for (b). The x-axis is defined as being directed into the page. The angle deviation of the NRs from the thickness direction (z-axis) is shown for the two different film samples in (c) and (d). See Figure 3 for axes directions.

It can be seen from Figure 5 and Figure 6 that there is a good dispersion of the NRs and NPLs in the PVB films both before (a) and after (b) stretching with the majority of particles being monodisperse with some small aggregates present. The z-axis (0°) and y-axis (90°) in the NPL films were identified by first finding the interface between the PVB/NPL film and the mounting resin. There was no visible interface for the NR samples however the thickness and stretching direction could be identified from the relative alignment of the NRs.

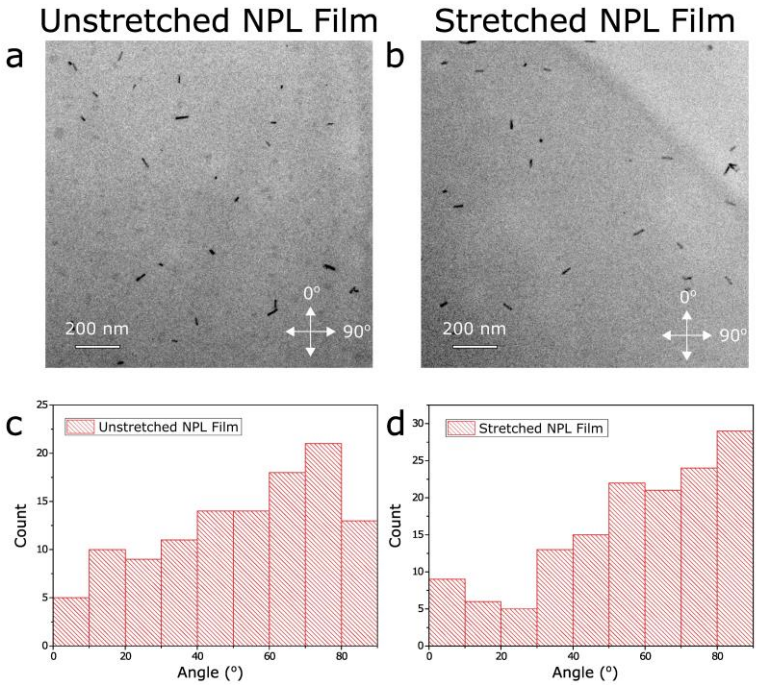

Figure 6. TEM images show representative cross-sectional areas of (a) an unstretched film containing CdSe/CdZnS NPLs (b) a stretched film containing the same nanocrystals. The axis labelled 0° is the thickness direction (z-axis) of the films whereas 90° is the direction which will be stretched (y-axis) for (a) and the stretch direction (y-axis) for (b). The x-axis is defined as being directed into the page. The angle deviation of the NPLs from the thickness direction (z-axis) is shown for the two different film samples in (c) and (d). See Figure 3 for axes directions.

There visually appears to be a bias in the alignment of the nanocrystals away from the z-axis in all the samples and to verify this a statistical analysis of the particle alignment was conducted on at least 100 particles over several images (Figure 5 and Figure 6 (c) and (d)). The absolute count differences between samples relates to the statistical sample size and does not relate to the density of particles within the samples. There is a distinct trend of nanocrystals being aligned away from the z-axis, shown in (c) and (d) of Figure 5 and Figure 6, for both samples with and without stretching. The alignment of the nanocrystals within the x-y plane, away from the z-axis, likely occurs as a result of the alignment of the polymer during the solvent drying process and has significant implications on the absorbance and light guiding of the films [52]. This observation agrees with previous 3D single-particle orientation measurements, which show that elongated nanocrystals were aligned within the x-y plane in solvent cast polymer films [39]. We can use the nanocrystal alignment observations to validate our conclusions about the absorbance data presented in Figure 4.

Using the statistical information from Figure 5 and Figure 6, we quantitatively analysed the nanocrystal alignment, shown in Figure 7. The nanocrystal counts from Figure 5 and Figure 6 were normalized and grouped into intervals of 30°, represented by the relative proportions shown in Figure 7 (a). It can be observed that the NR samples have a greater proportion of nanocrystals aligned greater than 60° compared to the NPL sample, both for unstretched and stretched samples. This indicates that the NRs are more susceptible to alignment than the NPLs, both during the drying process and during stretching. The change in orientation, shown in Figure 7 (b), was calculated by subtracting the relative proportion of the nanocrystal orientations before stretching from the value after stretching. The increase in nanocrystals with orientation greater than 60°, and conversely decrease in nanocrystals with orientation less than 30°, is a measure of how much the alignment increased after stretching. We observe that the alignment of the NPLs increased by a greater degree than the NRs during stretching, despite the overall lower alignment. This explains the larger increase in thickness corrected absorbance for the NPL sample, seen in Figure 4 (c).

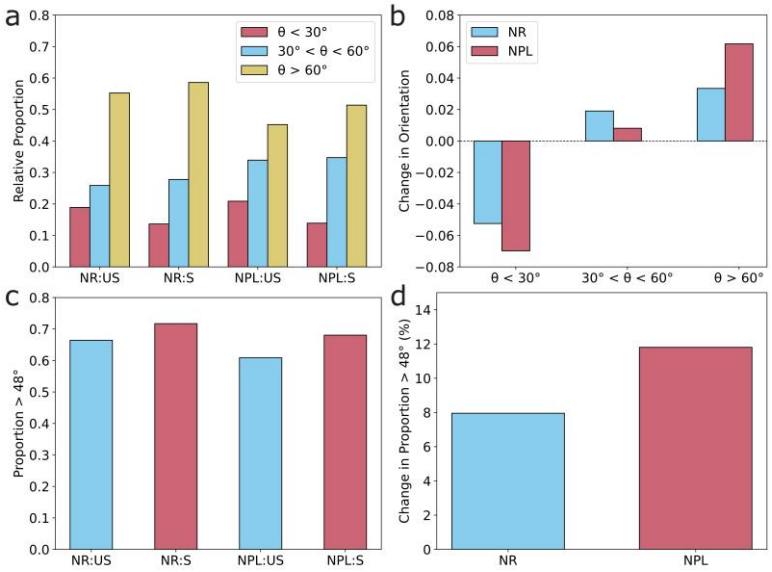

Figure 7. Quantitative analysis of the nanocrystal alignment. (a) The nanocrystal counts in Figure 5 and Figure 6 were normalized and the relative proportions grouped into intervals of 30° for the unstretched (US) and stretched (S), NR and NPL films, where θ is the angle relative to the thickness axis (z-axis). (b) Change in orientation (difference between relative proportions before and after stretching) for the NP and NPL films across the 30° intervals. (c) Proportion of nanocrystals aligned away from the z-axis by more than 48°, the critical angle for total internal reflection. (d) Percentage change in nanocrystals aligned away from the z-axis by more than 48° after stretching.

In addition to absorbance, the nanocrystal angle has consequences on the light guiding of the fluorescence in the films. PVB has a refractive index of 1.486 therefore when we apply Snell's law we obtain a critical angle for total internal reflection of 42° [53]. Considering that the majority of the fluorescence is directed perpendicular to the long axis for elongated nanocrystals, such as nanorods and elongated nanoplatelets, then there will be a significant decrease in total internal reflection for nanocrystals angled greater than 48° away from the z-axis, or from another perspective, for nanocrystals angled less than 42° away from the x-y plane [8]. Figure 7 (c) shows that the majority of both nanorods and nanoplatelets, stretched and unstretched, are higher than the critical angle therefore it is expected that light guiding will be reduced compared to randomly aligned nanocrystals or isotropic emitters. Furthermore, there was an 11.8% increase in NPLs aligned in an orientation unfavourable for TIR after stretching, compared with an 8.0% increase for NRs. This is advantageous for applications where light guiding should be avoided, such as liquid crystal displays, but a

disadvantage when light guiding is beneficial, such as for LSCs [1]. Studies have previously shown that fluorophores with anisotropic fluorescence produce the highest internal photon efficiencies in LSCs when aligned parallel to the z-axis ($\theta = 0^o$) [34].

When considering nanocrystal containing films for LSC applications, this means that drop casting produces non-optimal orientation for elongated nanocrystals, resulting in reduced light guiding and increased photon losses from the film face. Polymerisation methods can produce polymer films containing randomly oriented nanorods and therefore polymerisation should be the preferred fabrication method for minimizing escape cone losses [16]. Orienting the nanocrystals parallel to the z-axis would produce the highest internal photon efficiency but aligning fluorescent nanocrystals in this orientation for LSC applications is yet to be achieved [35, 37]. Orientation of elongated nanoplatelets has previously been observed while spin coating thin films and should also be investigated for other solvent evaporation methods such as doctor-blading to determine if the same orientation effect is present [8].

It should be noted that there was an observable difference between the distributions of the NPLs and NRs between angles of 80^o and 90^o. Specifically, the count for the unstretched NPL film between angles of 80^o and 90^o is lower than between angles of 70^o and 80^o or angles of 60^o and 70^o. Something not yet considered is the possibility of nanocrystals oriented towards the x-axis, perpendicular to both 90^o and 0^o, which on the TEM images would be observed as nanocrystals directed into the page. NPLs, which have a length, width and thickness, could present as a different angle when oriented into the page. When observing NPLS from this angle, the width of the NPL would be observed, rather than the length obscuring the true alignment of the particles. After the NPL sample is stretched, this is not observed which could indicate that there has been an alignment of NPLs from the x-axis towards the y-axis, denoted as 90^o. To investigate this effect and to better understand the optical effects of stretching the films, the fluorescence anisotropy was measured and analysed.

3.3. Fluorescence Anisotropy

The fluorescence anisotropy spatial maps of the QDs, NRs and NPLs in unstretched and stretched films are shown in Figure 8 (a) to (f). There is minimal change in fluorescence anisotropy of the QD sample after stretching seen by comparing Figure 8 (a) and (d). There was a significant increase in anisotropy for both the NR samples (b) & (e) and the NPL samples (c) & (f). In both Figure 8 (e) and (f) there are regions where the anisotropy is lower than the surrounding areas which is caused by micro-tears in the polymer film generated during stretching.

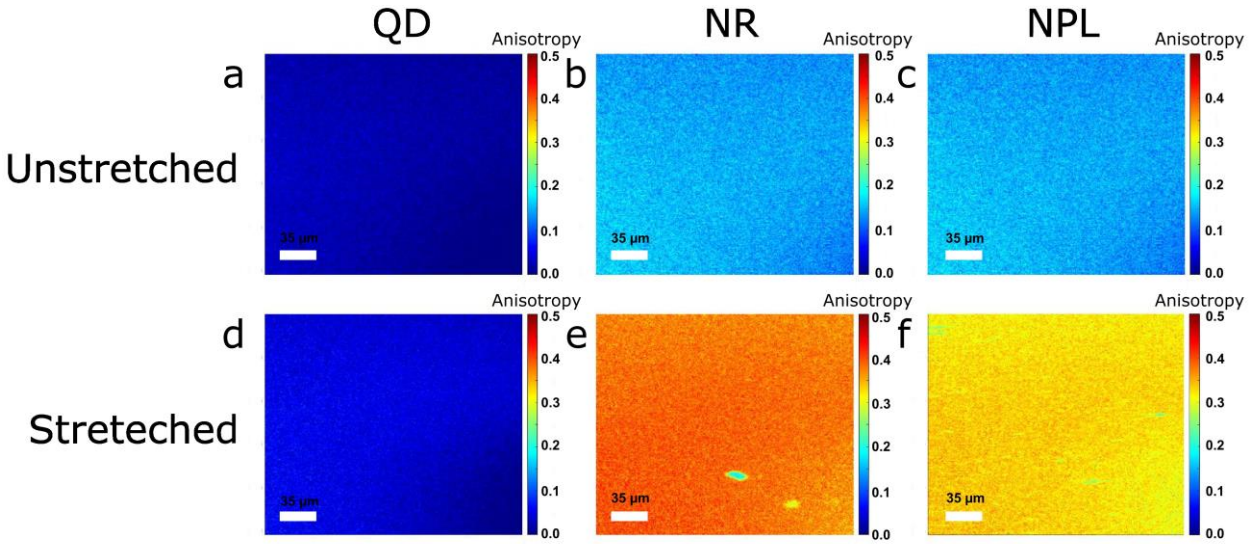

Figure 8. Fluorescence anisotropy (r) images calculated using Equation 2 on a pixel-by-pixel basis for unstretched PVB films containing (a) QDs, (b) NRs and (c) NPLs. Fluorescence anisotropy images of the three sample after stretching are shown in (d), (e) and (f).

The differences in fluorescence anisotropy can be better assessed when the pixels are statistically analysed and plotted. Figure 9 shows quantitatively the changes in fluorescence anisotropy after stretching for the QD film (a), NR film (b) and NPL film (c). As expected, there is a minimal change for the QD samples but significant shifts to higher anisotropy values for the NRs and NPLs after stretching.

While the TEM images in Figure 5 and Figure 6 do not show a significant change in the alignment of the nanocrystals relative to the z-axis after stretching, the fluorescence anisotropy results imply there is significant rotation of the NRs and NPLs around the z-axis, from the x-axis towards the y-axis (stretching direction), during stretching resulting in larger fluorescence anisotropy values. The QD particles are spherical, isotropic emitters and therefore, they are unable to be reoriented by elongational flow of the polymer. On the other hand, reorientation of the NRs and NPLs within the x-y plane of the film towards the y-axis (stretching direction) has occurred. The NPLs, despite having a significantly different geometry to the NRs, have similar polarisation properties. This has been previously attributed to quantum confinement of the exciton in the smaller lateral direction leading to linearly polarised light being emitted parallel to the long direction of the NPL [1].

The results obtained here in polymer films indicate the alignment mechanisms of the two types of nanocrystals are similar. It can also be seen that both the NRs and NPLs have a fluorescence anisotropy of approximately 0.15 in unstretched films, consistent with previous reports that these types of nanocrystals, when randomly dispersed, display wavelength dependent anisotropy values between 0.05 - 0.15 [1, 54].

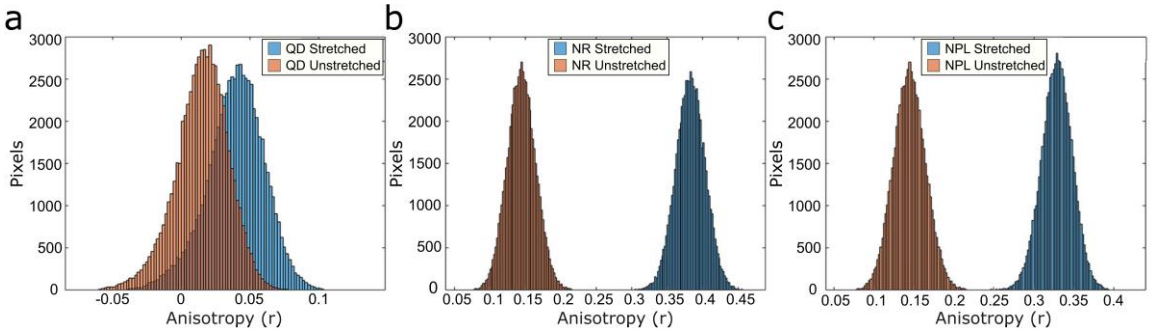

Figure 9. Statistical analysis of fluorescence anisotropy values for the unstretched and stretched films for a) QDs, b) NRs and c) NPLs.

3.4. Fluorescence Anisotropy – True Strain Relationship

The fluorescence anisotropy – strain relationship can be investigated further by determining the degree of fluorescence anisotropy change as a function of the film true strain. A previous study has also reported the fluorescence polarisation increase from stretching polymer films containing elongated nanocrystals, however only two elongation conditions (unstretched and at 400% elongation) were investigated warranting further study [1]. The fluorescence anisotropy of a PVB film containing NPLs was measured at a range of true strain values between 0 and 1.58 (485% elongation). A stretched PVB sample demonstrating the strain measurement technique is shown in Figure 10 (a). Unlike the example sample in Figure 10 (a), the test specimens containing NPLs maintained perfectly parallel markings in the x-axis direction after stretching indicating that the true strain between each set of lines in the y-axis direction was equal across the width of the film.

The strain measurements were then correlated with fluorescence anisotropy, measured using scanning

confocal microscope, at each section of the stretched film with the relationship between strain and anisotropy shown in Figure 10 (b). This relationship was modelled as an exponential function, given by Equation 5.

$$r = -ae^{-b\epsilon} + c \quad \text{(Equation 5)}$$

where r is fluorescence anisotropy, ε is true strain and a, b and c are fitting parameters.

While the equation is empirical, the fitting parameters represent properties of the system. The parameter c represents the theoretical maximum achievable fluorescence anisotropy from alignment, as the term $-ae^{-b\varepsilon}$ approaches 0 as ε tends to infinity. The y-intercept of the model is equal to c – a, as the term $-ae^{-b\varepsilon} = -a$ when true strain is equal to zero. The term b dictates the exponential decay towards the maximum fluorescence anisotropy. The best fit of the non-linear function was determined with an in-house developed open-source Python tool [55]. Limits were imposed on the parameters to ensure convergence of the regression. The fitting parameter limits are as follows: $-0.5 < c < 1$ to ensure that r can only take values between -0.5 and 1, $0 < a < 1$ to ensure also that the y-intercept is between -0.5 and 1 and $0 < b < \infty$ to ensure that the exponential model shape cannot be inverted. The line of best fit utilised parameters: a = 0.34, b = 1.12 and c = 0.52. The R^2 of this fit was 0.994 and the residuals were randomly distributed across the whole set of strain values, see Figure S15 (b). This implies that the maximum fluorescence anisotropy that can be achieved by alignment in our particular NPL/PVB system is 0.52, which is lower than has been achieved using certain organic dyes in stretched films [56].

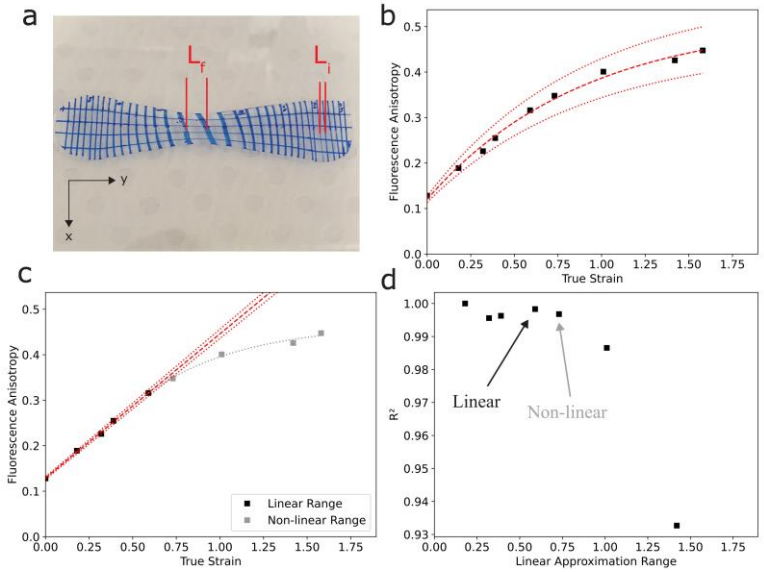

Figure 10. (a) an example of the strain measurement method using a PVB sample without NPLs. The initial (L_i) and final (L_f) lengths are required to calculate true strain (ε) in the y-axis direction using Equation 1. (b) Fluorescence anisotropy and true strain data for a stretched PVB film containing NPLs. An exponential model was applied to the data using Equation 5. The red dotted lines represent the model after using the 95% confidence limits of modelling parameters a and c. (c) A linear approximation has been applied between true strain values of 0 and 0.59 (red dashed line). The red dotted lines represent the standard error of the slope and intercept of the linear fit. (d) R^2 values of the range linear fits with true strain upper limits between 0.18 and 1.42.

While the use of an exponential model is well justified to fit the data, linear responses are preferred for sensor calibration. As a result, we investigated whether a subset of the data could justifiably be approximated as a linear model. To determine the best range over which to apply a linear approximation, linear regression was

applied to the data from 0 to a range of true strain values from 0.18 (120% elongation) up to 1.42 (414% elongation). The full range of linear regression fits and associated residual plots are presented in the Supporting Information (Figure S7-S13).

The R^2 values of all the linear approximations using data from 0 true strain to a range of end strain values between 0.18 and 1.42 are shown in Figure 10 (d). All the linear regression models up to a true strain of 0.73 have very high R^2 values (> 0.995), but it is insufficient to assess approximation validity with R^2 alone. The linear model with the true strain range of 0 to 0.58 (178% elongation), shown in Figure 10 (b), exhibited an R^2 value of 0.998 and a random residual plot, shown in Figure S11 (b), confirming this model is an appropriate approximation for the initial strain region. When the linear approximation was extended between the true strain range of 0 and 0.73 (207% elongation), the residual plot showed a distinct curvature indicating that a linear approximation is no longer appropriate, shown in Figure S12 (b). Consequently, this approximation was labelled as "Non-linear" on Figure 10 (d).

If engineering strain is used instead of true strain, as investigated in previous studies, the fluorescence anisotropy cannot be justifiably approximated at the same degree of film deformation [21]. The R^2 value drops to 0.989 for the range of true strain 0 to 0.58, after true strain values are converted to engineering strain, see Figure S14 (a). Furthermore, the residuals show a curved pattern indicating that the fluorescence anisotropy – engineering strain data is non-linear, see Figure S14 (b).

Due to strong statistical evidence supporting the use of a linear approximation up to moderate strains, the true strain of a region of the film can be interpolated using the fluorescence anisotropy value in that region of the film. We propose that elongated nanocrystals such as elongated NPLs and NRs in films are appropriate to be used to measure uniaxial true strain which could occur during polymer processing [18]. This fluorescence anisotropy system is a non-destructive test method and the strain of a film can be monitored with spatial resolution on the micron scale. Additionally, this method allows the strain to be monitored without any electrical input or physical contact. Rather, strain can be measured using an excitation light source, polarisation filters and a detector at the nanocrystal emission wavelength [18].

Additional validation work would be required to determine if the empirical relationship holds for other polymer films, for other nanocrystals and geometries and to determine the ultimate sensitivity at small strains. It has been shown that nanocrystals with different sizes and aspect ratios have different degrees of polarisation at 400% elongation and therefore the alignment of nanocrystals is dependent on nanocrystal geometry as well as strain [1]. The exponential model projects a maximum fluorescence anisotropy of 0.52 for the NPLs in the stretched film however different nanocrystal shapes and sizes may modify the projected maximum fluorescence anisotropy, warranting further investigation. We hypothesise that different nanocrystals will likely result in linear approximations with different gradients and different maximum strains at which the fluorescence anisotropy – strain relationship can no longer be approximated as linear. Based on the degree of alignment, smaller nanocrystals should produce steeper gradients with a smaller range of strains where the data is approximately linear resulting in greater sensitivity, while larger nanocrystals will be less sensitive but will be usable over a larger range of true strain values [1].

Unlike fluorescent dye molecules which have fixed structures, the size and aspect ratio of elongated nanocrystals can be controlled, therefore the sensitivity is more tuneable compared with fluorescent dyes. An additional advantage that elongated fluorescent nanocrystals have over organic dyes is that their fluorescence spectra are tuneable with size and composition, with possible peak emission ranging from near the UV-visible boundary to near infrared (NIR) [57-59]. Moreover, luminescent nanocrystals have the potential for greater photostability than organic dyes [60]. A more detailed study of this fluorescence anisotropy – strain relationship is required to investigate these mechanisms with a range of different nanocrystals with varied sizes and aspect ratios. Understanding this mechanism will also assist with producing nanocrystal films with controlled polarisation properties for a range of other applications including LCD displays [1].

3.5. *Light Guiding Efficiency*

To investigate the effect of the observed nanocrystal alignment on light guiding in the films, the methods and terminology from the LSC field have been adopted [25]. Internal photon efficiency (η_{int}) is a particularly useful metric for comparing photon trapping between different fluorophore systems and different samples because it is independent of the amount of light absorbed, which can vary with absorption properties of the luminophore or concentration. The internal photon efficiency requires edge efficiency and the film PLQY to be measured, as is evident in Equation 3.

It can be seen from Figure 11 (a) that when the PVB samples containing nanocrystals are stretched there was a small decrease in PLQY for all three particle types. After stretching, the PLQY decreased from 0.53 to 0.48 for QDs, from 0.75 to 0.69 for NRs and from 0.76 to 0.70. This may be due to the additional processing step, which involved heating the films during stretching, introducing some non-radiative traps, although the effect is small. The QDs displayed the lowest PLQY values, with the nanorods and nanoplatelets performing better. Prior to casting the films, the PLQY values of the nanocrystals in solvent were 0.52, 0.69 and 0.77 for the QDs, NRs and NPLs respectively. Therefore, we conclude that the film casting process did not significantly decrease the PLQY of the nanocrystals. The PLQY for each of the three types of nanocrystals may be improved by optimisation of the synthesis but this was not pursued in this study. From the edge efficiency (η_{edge}) results, seen in Figure 11 (b), we can observe the effect of different light guiding mechanisms in the film.

The edge efficiency was defined in Equation 4 as the ratio of edge emitted photons to photons emitted from all the film faces and edges. It is apparent that the QDs exhibit the highest η_{edge}, NRs the second highest and NPLs the lowest. The unstretched nanorod film had an η_{edge} that was 19.4% lower than the unstretched QD film, while the unstretched nanoplatelet was 32.9% lower. Similarly with the stretched films, the NR film was 20.6% lower than the QD film while the NPL film was 35.7% lower than the QD film. Previous emission and absorption data in Figure 4 (a) and (b) shows that the QDs and NRs have very similar optical properties and therefore we can conclude that the reduction in η_{edge} is predominantly due to alignment of the nanorods away from the z-axis direction, the optimal angle for maximizing η_{edge} for elongated nanocrystals. The efficiency of the nanoplatelets has an even greater reduction in η_{edge} relative to the QD film due to a combination of suboptimal alignment and additional reabsorption losses derived from the overlap of the emission and absorption spectra observed in Figure 4 (c).

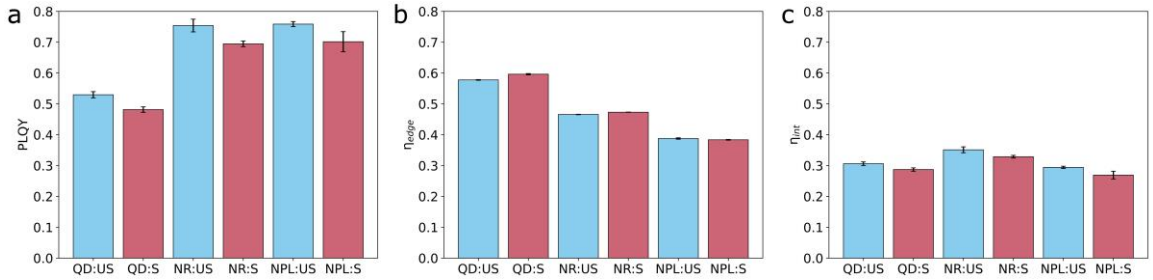

Figure 11. (a) Photoluminescence quantum yield (PLQY), (b) edge efficiency (η_{edge}) and (c) internal photon efficiency (η_{int}) measurements of fluorescent nanocrystals in unstretched (US) and stretched (S) PVB films.

It can also be observed that the three samples have slightly different responses of η_{edge} to stretching of the films. The QDs have a 3.2 % increase in η_{edge} and the NRs have a 1.6 % increase in η_{edge} while the NPLs have a 1.1 % decrease in η_{edge} after stretching. Stretching of the film has two main effects on the η_{edge} of films. Firstly, there is a decrease in the thickness of the films which results in a decrease in the absorbance of the

film. This decrease in absorbance is a result of a decrease in the total number of nanocrystals in the 1 cm x 1 cm test samples as the stretching redistributes the nanocrystals over a large lateral area. The lower absorbance reduces fluorescence reabsorption within the film and hence increases the η_{edge}. This effect applies to all three nanocrystal types. For the elongated nanocrystals, the stretching also results in an alignment away from the z-axis (thickness direction), which increases the escape cone losses and hence decreases η_{edge}. The results show that the QDs had the greatest increase in η_{edge} due to the thickness reduction effect and no effect of the alignment. The NRs experienced both effects, but the alignment change was small, resulting in a slight increase in η_{edge}. The NPLs had the greatest change in alignment which was sufficient to counteract the effect of the thickness decrease, and the net effect was a small decrease in η_{edge}.

The internal photon efficiency (η_{int}) results are shown in Figure 11 (c). These were calculated as the product of PLQY and η_{edge} and therefore reflect a combination of the trends observed in PLQY and η_{edge}. The lower PLQY result of the QD films could not offset the higher η_{edge} value and therefore η_{int} was lower than for the NR films. The NPL films have the lowest η_{int} values largely due to the low edge efficiency. Removing the effect of PLQY, which is largely derived from the PLQY of the nanocrystals, we can conclude that the QD film has the greatest guiding of light to the edges of the film, whereas alignment of the NRs and NPLs during the drop casting process has resulted in a decrease in light guiding and hence an increase the light emitted from the faces. Using this information one can tailor the choice of nanocrystal to the application for the nanocrystal film. Applications where light emission from the face of the film is preferred, such as displays, benefit from the use of elongated nanocrystals due to their natural alignment during casting. On the other hand, QDs are preferred for cast films where light guiding to the edges is preferred such as LSCs [6]. The best-case scenario for light guiding to the film edges is expected when elongated nanocrystals are aligned parallel to the z-axis, however this has yet to be demonstrated in practice [35, 37].

3.6. Monte Carlo Ray-Tracing Simulations

The experimental results showed that the NRs were aligned away from the z-axis and the edge efficiency of the NRs was lower than for QDs. Monte Carlo simulations were performed to demonstrate a causal relationship between the NR alignment and the decrease in edge efficiency. Simplified models of the NR angle distributions in the films were used due to the complexity of the angle distribution of the NRs in the TEM images shown in Figure 5 and Figure 6. The unstretched NR film was modelled with the angles of the NRs distributed randomly within the x-y plane, hence perfectly perpendicular to the z-axis, while the stretched NR film was modelled with the NRs perfectly aligned in the y-axis (stretching) direction. These assumptions are useful in demonstrating that the differences in light guiding efficiencies between QD and NR films observed in experiments are related to fluorescence loss from the film faces due to alignment of NRs away from the z-axis. The simulations assumed the nanocrystals to have PLQY values equal to the solution PLQY values of the particles, which were 0.52 and 0.64 for the QDs and NRs respectively.

The simulated PLQY values in Figure 12 (a) can be compared with the experimental values in Figure 11 (a). The values are in good agreement because the simulations used the experimental PLQY values of the nanocrystals in solution as model inputs. The simulations show an increase in PLQY upon stretching, which is opposite to the decrease observed experimentally. This indicates that the experimental decrease is due to an effect not taken into account in the simulations, i.e. consistent with our interpretation above that it is due to non-radiative traps introduced during hot stretching of the films.

Comparing the edge efficiencies obtained via simulation and experiment shows that the model overestimates the efficiency of the device at light guiding photons to the edge. There are many factors which are not accounted for which can explain why the experimental edge efficiencies are lower. The simulations assume the film surfaces are perfectly flat, however in reality film surfaces have a degree of roughness which can scatter some light during the light guiding process. There are also defects in the matrix polymer films which

can scatter light and reduce the light guiding process. These factors can be expected to lower edge efficiencies for the experimental data relative to the Monte Carlo simulations. Furthermore, the effect of birefringence during stretching was not accounted for in the simulations, which may introduce to additional uncertainty. Birefringence in PVB films has been shown to be approximately 0.014 at elongations approaching 400% [61]. PVB has a refractive index of 1.486 therefore to estimate the maximum effect of birefringence we can examine the critical angle for PVB between the refractive index bounds 1.472 to 1.500 [53]. The critical angle for a refractive index of 1.472 is 42.8° while it is 41.8° for refractive index of 1.500. Considering that the simulations assume that the NRs are aligned in the x-y plane, accounting for birefringence will not affect the NR results, however birefringence may affect the uncertainty in the QD results by a small degree.

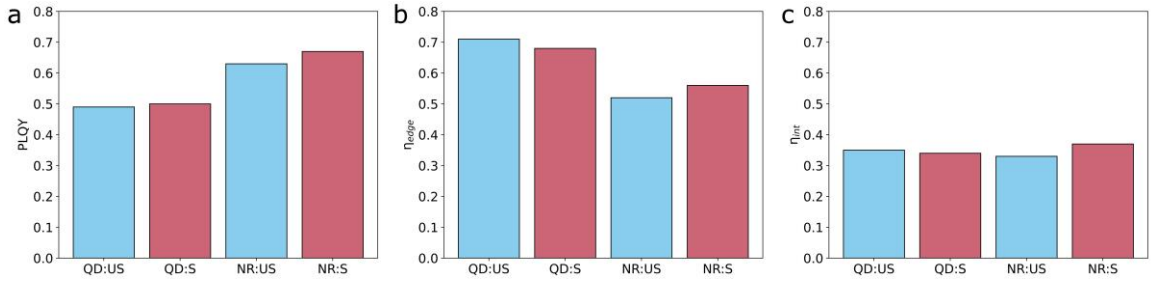

Figure 12. Monte Carlo simulation results for (a) PLQY, (b) η_{edge} and (c) η_{int} values for unstretched (US) and stretched (S) QD and NR films.

The most important conclusion that can be drawn from the data is that the decrease in edge efficiency observed between the experimental QD and NR samples is also observed in the simulations. The absorption and fluorescence spectra in Figure 4 (a) and (b), used as inputs to the simulations, are substantially similar in shape and therefore the primary difference between the samples is the alignment of the NRs. This supports our conclusion that the primary cause for the decrease in edge efficiency of the experimental NR films is the alignment of the NRs away from the z-axis. A recent study claimed that a stretched polymer film containing NRs exhibited reduced escape cone losses and improved LSC collection efficiencies, however the present study clearly demonstrates that the NR alignment resulting from PVB film stretching is not optimal for light guiding to the film edges [35].

The internal photon efficiency (η_{int}) results, shown in Figure 12 (c), are the product of the PLQY and edge efficiency and therefore the trends follow the trends of the PLQY and edge efficiency. For this reason, the internal photon efficiency is a less useful metric of comparison. Nonetheless, it can be noted that the simulated η_{int} values for QDs and NRs are similar due to the QD films having lower PLQY and the NR films having lower edge efficiency.

4. Conclusions

The effects of nanocrystal alignment on a range of film optical properties were investigated, including absorbance, fluorescence anisotropy and light guiding. Thickness corrected absorbance increased after stretching for NR and NPL films which was correlated with increased nanocrystal alignment in TEM cross-section images. Fluorescence anisotropy measurements showed that the fluorescence of the NR and NPL films became highly polarised after stretching consistent with prior studies of elongated nanocrystals in polymer films [1]. The present study further determined that there is an exponential relationship between fluorescence anisotropy and true strain for the NPL film, and that the relationship can be approximated as linear up to moderate true strain values. With this knowledge, we propose that films containing elongated nanocrystals such as NRs and NPLs could be utilised to measure strain in films, where localised strain can be measured on a microscopic length scale. Further work is required to investigate the effect for different nanocrystal types, sizes and aspect ratios and determine the sensitivity that can be achieved with this

technique.

NR and NPL alignment during film casting and stretching resulted in increased fluorescence emission from the film faces, hence reduced light guiding. While beneficial for some applications, such as LCD displays, the alignment of NRs and NPLs during the drop casting process limits the potential of drop cast NR and NPL thin films for LSC applications [6]. The edge efficiency of QDs outperformed both NRs and NPLs in this study due to the random orientation of the QDs that results in isotropic fluorescence, rather than fluorescence biased towards the films faces. The use of drop casting should be avoided for elongated nanocrystal films where light guiding is required unless the nanocrystals can by simultaneously aligned towards the z-axis (thickness direction). The effect of other solvent casting techniques, such as doctor blading, on nanocrystal alignment should be investigated to determine if the light guiding of nanocrystal films made using these techniques is similarly affected. Monte Carlo ray-tracing simulations of a simplified system confirmed that the observed increase in fluorescence from the film faces was a result of alignment towards the plane in the NR film. Developing reliable methods to align NRs and NPLs in the correct geometry could increase the conversion efficiency of LSC devices.

5. CRediT authorship contribution statement

Timothy Warner: - Writing – original draft, Investigation, Formal analysis, Data curation, Conceptualisation, Methodology, Validation, Visualisation. **Michael Rinaudo:** Conceptualisation, Methodology, Software, Validation, Investigation, Writing – original draft. **Yang Xu:** Methodology, Formal Analysis, Investigation, Writing – original draft. **Jiho Han:** Resources, Writing – original draft, Writing – Review and Editing. **Arun Ashokan:** Resources, Writing – Review and Editing. **Nicholas Kirkwood:** Resources, Writing – Review and Editing. **Asaph Widmer-Cooper:** Conceptualisation, Writing – Review and Editing, Supervision, Funding acquisition. **Trevor A. Smith:** Writing – Review and Editing, Supervision, Funding Acquisition. **Kenneth P. Ghiggino:** Conceptualisation, Writing – Review and Editing, Supervision, Funding acquisition. **Gary Rosengarten:** Conceptualisation, Writing – Review and Editing, Supervision, Funding acquisition.

6. Declaration of competing interest

The authors declare that they have no known competing financial interests or personal relationships that could have appeared to influence the work reported in this paper.

7. Funding Information

This research was supported by the ARC Centre of Excellence in Exciton Science (CE170100026). Responsibility for the views, information, or advice expressed herein is not accepted by the Australian Government.

Acknowledgements

TEM characterisation and associated film sample preparation was performed at the Ian Holmes Imaging Centre, Bio21 Institute at the University of Melbourne. We thank Zlatan Trifunovic for assistance with TEM sample preparation and Assoc. Prof. Sergey Rubanov for assistance with TEM training and imaging. Computational resources were provided by the Sydney Informatics Hub, a Core Research Facility of the University of Sydney.

ORCID iDs

Timothy Warner: https://orcid.org/0000-0002-1141-2196
Yang Xu: https://orcid.org/0000-0003-1658-0313

Jiho Han: https://orcid.org/0000-0001-5306-5957
Nicholas Kirkwood: https://orcid.org/0000-0002-7845-7081
Asaph Widmer-Cooper: https://orcid.org/0000-0001-5459-6960
Trevor A. Smith: https://orcid.org/0000-0003-4453-9713
Kenneth P. Ghiggino: https://orcid.org/0000-0001-6621-4448
Gary Rosengarten: https://orcid.org/0000-0003-1327-5321

Data Availability Statement

The data that support the findings of this study are openly available in the figshare research repository https://doi.org/10.6084/m9.figshare.27901611 [62].

References

1. Cunningham, P.D., et al., *Assessment of Anisotropic Semiconductor Nanorod and Nanoplatelet Heterostructures with Polarized Emission for Liquid Crystal Display Technology*. ACS Nano, 2016. **10**(6): p. 5769-5781 DOI: 10.1021/acsnano.5b07949.
2. Nozik, A.J., *Quantum dot solar cells.* Physica E: Low-dimensional Systems and Nanostructures, 2002. **14**(1): p. 115-120 DOI: https://doi.org/10.1016/S1386-9477(02)00374-0.
3. Li, Z., et al., *Rapid and sensitive detection of protein biomarker using a portable fluorescence biosensor based on quantum dots and a lateral flow test strip.* Analytical chemistry, 2010. **82**(16): p. 7008-7014
4. Konstantatos, G., et al., *Ultrasensitive solution-cast quantum dot photodetectors.* Nature, 2006. **442**(7099): p. 180-183
5. Purcell-Milton, F. and Gun'ko, Y.K., *Quantum dots for Luminescent Solar Concentrators.* Journal of Materials Chemistry, 2012. **22**(33): p. 16687-16697 DOI: 10.1039/C2JM32366D.
6. Kim, W.D., et al., *Pushing the Efficiency Envelope for Semiconductor Nanocrystal-Based Electroluminescence Devices Using Anisotropic Nanocrystals.* Chemistry of Materials, 2019. **31**(9): p. 3066-3082 DOI: 10.1021/acs.chemmater.8b05366.
7. García de Arquer, F.P., et al., *Semiconductor quantum dots: Technological progress and future challenges.* Science, 2021. **373**(6555): p. eaaz8541
8. Yuan, G., et al., *Tuning the Photoluminescence Anisotropy of Semiconductor Nanocrystals.* ACS Nano, 2023. **17**(19): p. 19109-19120 DOI: 10.1021/acsnano.3c05214.
9. Yoon, D.-E., et al., *Origin of Shape-Dependent Fluorescence Polarization from CdSe Nanoplatelets.* The Journal of Physical Chemistry C, 2017. **121**(44): p. 24837-24844 DOI: 10.1021/acs.jpcc.7b07216.
10. Gordon, C.K., et al., *Heterostructured Nanotetrapod Luminophores for Reabsorption Elimination within Luminescent Solar Concentrators.* ACS Applied Materials & Interfaces, 2023. **15**(14): p. 17914-17921 DOI: 10.1021/acsami.3c01222.
11. Rodrigues, A.V., Onishi, B.S.D., and Ribeiro, S.J.L., *Facile Formation of Sulfurized Nanorod-Like ZnO/Zn(OH)2 and Hierarchical Flower-Like γ-Zn(OH)2/ϵ-Zn(OH)2 from a Green Synthesis and Application as Luminescent Solar Concentrator.* ChemPhysChem, 2023. **24**(21): p. e202300134 DOI: https://doi.org/10.1002/cphc.202300134.
12. Mauser, C., et al., *Anisotropic optical emission of single CdSe/CdS tetrapod heterostructures: Evidence for a wavefunction symmetry breaking.* Physical Review B, 2008. **77**(15): p. 153303 DOI: 10.1103/PhysRevB.77.153303.

13. Boyne, D.A., et al., *Process induced alignment of gold nano-rods (GNRs) in thermoplastic polymer composites with tailored optical properties.* Polymer, 2017. **110**: p. 250-259 DOI: https://doi.org/10.1016/j.polymer.2016.12.059.
14. Murphy, C.J. and Orendorff, C.J., *Alignment of Gold Nanorods in Polymer Composites and on Polymer Surfaces.* Advanced Materials, 2005. **17**(18): p. 2173-2177 DOI: 10.1002/adma.200501042.
15. He, J., et al., *In situ synthesis and macroscale alignment of CsPbBr3 perovskite nanorods in a polymer matrix.* Nanoscale, 2018. **10**(33): p. 15436-15441 DOI: 10.1039/C8NR04895A.
16. Gripp, N.J., *Alignment of CdSe/CdS Nanoparticles in UV-Curable Resin for Applications in Luminescent Solar Concentrators.* Texas A&M University, 2019. **Master's thesis** DOI: https : / /hdl .handle .net /1969 .1 /186285.
17. Xu, Y., et al., *Resolving conjugated polymer film morphology with polarised transmission and time-resolved emission microscopy.* Methods and Applications in Fluorescence, 2024. **12**(3): p. 035004 DOI: 10.1088/2050-6120/ad388f.
18. Bur, A.J., Roth, S.C., and Thomas, C.L., *Fluorescence anisotropy sensor and its application to polymer processing and characterization.* Review of Scientific Instruments, 2000. **71**(3): p. 1516-1523 DOI: 10.1063/1.1150499.
19. Bur, A.J. and Roth, S.C., *Real-time monitoring of fluorescence anisotropy and temperature during processing of biaxially stretched polypropylene film.* Polymer Engineering & Science, 2004. **44**(4): p. 805-813 DOI: https://doi.org/10.1002/pen.20072.
20. Bur, A.J., et al., *Observations of shear-induced molecular orientation in a polymer melt using fluorescence anisotropy measurements.* Macromolecules, 1991. **24**(12): p. 3715-3717
21. Bur, A.J., et al., *Fluorescence anisotropy measurements on a polymer melt as a function of applied shear stress.* Macromolecules, 1992. **25**(13): p. 3503-3510
22. Roberts, D.R.T. and Holder, S.J., *Mechanochromic systems for the detection of stress, strain and deformation in polymeric materials.* Journal of Materials Chemistry, 2011. **21**(23): p. 8256-8268 DOI: 10.1039/C0JM04237D.
23. Jameson, D.M. and Ross, J.A., *Fluorescence Polarization/Anisotropy in Diagnostics and Imaging.* Chemical Reviews, 2010. **110**(5): p. 2685-2708 DOI: 10.1021/cr900267p.
24. Ramachandran, A.M., et al., *A comprehensive review on optics and optical materials for planar waveguide-based compact concentrated solar photovoltaics.* Results in Engineering, 2022. **16**: p. 100665 DOI: https://doi.org/10.1016/j.rineng.2022.100665.
25. Warner, T., Ghiggino, K.P., and Rosengarten, G., *A critical analysis of luminescent solar concentrator terminology and efficiency results.* Solar Energy, 2022. **246**: p. 119-140 DOI: https://doi.org/10.1016/j.solener.2022.09.011.
26. Weber, W.H. and Lambe, J., *Luminescent greenhouse collector for solar radiation.* Applied Optics, 1976. **15**(10): p. 2299-2300 DOI: 10.1364/AO.15.002299.
27. Debije, M.G. and Verbunt, P.P.C., *Thirty Years of Luminescent Solar Concentrator Research: Solar Energy for the Built Environment.* Advanced Energy Materials, 2012. **2**(1): p. 12-35 DOI: 10.1002/aenm.201100554.
28. Wei, M., et al., *Ultrafast narrowband exciton routing within layered perovskite nanoplatelets enables low-loss luminescent solar concentrators.* Nature Energy, 2019. **4**(3): p. 197-205 DOI: 10.1038/s41560-018-0313-y.
29. Goetzberger, A. and Greube, W., *Solar energy conversion with fluorescent collectors.* Applied physics, 1977. **14**(2): p. 123-139 DOI: 10.1007/BF00883080.
30. Li, H., et al., *Doctor-blade deposition of quantum dots onto standard window glass for low-*

loss large-area luminescent solar concentrators. Nature energy, 2016. **1**(12): p. 16157 DOI: 10.1038/nenergy.2016.157.
31. Meinardi, F., et al., *Large-area luminescent solar concentrators based on 'Stokes-shift-engineered' nanocrystals in a mass-polymerized PMMA matrix.* Nature photonics, 2014. **8**(5): p. 392-399 DOI: 10.1038/nphoton.2014.54.
32. Warner, T., et al., *Reducing Quantum Dot Aggregation in Luminescent Solar Concentrators*, in *Asia-Pacific Solar Research Conference*. 2019, Australian PV Institute (APVI): Canberra DOI: https://doi.org/10.6084/m9.figshare.27922785.
33. Hill, S.K.E., et al., *Silicon Quantum Dot–Poly(methyl methacrylate) Nanocomposites with Reduced Light Scattering for Luminescent Solar Concentrators.* ACS Photonics, 2019. **6**(1): p. 170-180 DOI: 10.1021/acsphotonics.8b01346.
34. Zhang, B., et al., *Highly Efficient Luminescent Solar Concentrators by Selective Alignment of Donor–Emitter Fluorophores.* Chemistry of Materials, 2019. **31**(8): p. 3001-3008 DOI: 10.1021/acs.chemmater.9b00647.
35. Moraitis, P., et al., *Should Anisotropic Emission or Reabsorption of Nanoparticle Luminophores Be Optimized for Increasing Luminescent Solar Concentrator Efficiency?* Solar RRL, 2020. **4**(10): p. 2000279 DOI: https://doi.org/10.1002/solr.202000279.
36. van der Burgt, J.S., et al., *Unlocking Higher Power Efficiencies in Luminescent Solar Concentrators through Anisotropic Luminophore Emission.* ACS Applied Materials & Interfaces, 2021. **13**(34): p. 40742-40753 DOI: 10.1021/acsami.1c12547.
37. Wilfried, G.J.H.M.V.S., et al. *Strategies for the optimization of color neutral, transparent, and efficient luminescent solar concentrators*. in *Proc.SPIE*. 2023.
38. Fisher, M., et al., *Utilizing vertically aligned CdSe/CdS nanorods within a luminescent solar concentrator.* Applied physics letters, 2015. **106**(4): p. 41110 DOI: 10.1063/1.4906460.
39. Liu, X., et al., *Highly Efficient and Stable Luminescent Solar Concentrator Based on Light-Harvesting and Energy-Funneling Nanodot Pools Feeding Aligned, Light-Redirecting Nanorods.* Solar RRL. **n/a**(n/a): p. 2400273 DOI: https://doi.org/10.1002/solr.202400273.
40. Fan, F., et al., *Continuous-wave lasing in colloidal quantum dot solids enabled by facet-selective epitaxy.* Nature, 2017. **544**: p. 75-79 DOI: https://doi.org/10.1038/nature21424.
41. Carbone, L., et al., *Synthesis and Micrometer-Scale Assembly of Colloidal CdSe/CdS Nanorods Prepared by a Seeded Growth Approach.* Nano Letters, 2007. **7**(10): p. 2942-2950 DOI: 10.1021/nl0717661.
42. Bertrand, G.H.V., et al., *Shape control of zincblende CdSe nanoplatelets.* Chemical Communications, 2016. **52**(80): p. 11975-11978 DOI: 10.1039/C6CC05705E.
43. Rossinelli, A.A., et al., *Compositional Grading for Efficient and Narrowband Emission in CdSe-Based Core/Shell Nanoplatelets.* Chemistry of Materials, 2019. **31**(22): p. 9567-9578 DOI: 10.1021/acs.chemmater.9b04220.
44. Warner, T., *Dispersion and alignment of semiconductor nanocrystals for luminescent solar concentrators*, in *Doctoral Thesis*. 2022, RMIT University DOI: https://doi.org/10.25439/rmt.27595536.
45. Meinardi, F., et al., *Doped Halide Perovskite Nanocrystals for Reabsorption-Free Luminescent Solar Concentrators.* ACS Energy Letters, 2017. **2**(10): p. 2368-2377 DOI: 10.1021/acsenergylett.7b00701.
46. Faridmehr, I., Hodjati, R., and Azimi, M., *Correlation between engineering stress-strain and true stress-strain curve.* American Journal of Civil Engineering and Architecture, 2014. **2**(1): p. 53-59

47. Zhang, B., et al., *A luminescent solar concentrator ray tracing simulator with a graphical user interface: features and applications.* Methods and applications in fluorescence, 2020. **8**(3): p. 37001-037001 DOI: 10.1088/2050-6120/ab993d.
48. Rinaudo, M., *Nanorods in Luminescent Solar Concentrators: Optical Modelling and Self-Assembly Strategies*, in *Doctoral Dissat*. 2023, The University of Sydney
49. Yuan, G., et al., *Angular distribution of polarized spontaneous emissions and its effect on light extraction behavior in InGaN-based light emitting diodes.* Journal of Applied Physics, 2014. **115**(9): p. 093106 DOI: 10.1063/1.4867401.
50. Kamal, J.S., et al., *Direct determination of absorption anisotropy in colloidal quantum rods.* Physical review. B, Condensed matter and materials physics, 2012. **85**(3): p. 035126 DOI: 10.1103/PhysRevB.85.035126.
51. Mohammadimasoudi, M., Hens, Z., and Neyts, K., *Full alignment of dispersed colloidal nanorods by alternating electric fields.* 2016 DOI: 10.1039/c6ra02620f.
52. Prest, W.M. and Luca, D.J., *The alignment of polymers during the solvent-coating process.* Journal of Applied Physics, 1980. **51**(10): p. 5170-5174 DOI: 10.1063/1.327464.
53. Tsugawa, N., Ito, A., and Yamaguchi, M., *Effect of lithium salt addition on the structure and optical properties of PMMA/PVB blends.* Polymer, 2018. **146**: p. 242-248 DOI: https://doi.org/10.1016/j.polymer.2018.05.042.
54. Ratnaweera, R.J., et al., *Quantifying Order during Field-Driven Alignment of Colloidal Semiconductor Nanorods.* ACS Nano, 2022. **16**(3): p. 3834-3842 DOI: 10.1021/acsnano.1c08488.
55. Warner, T. and Takhsha, N., *Tool for modelling relationship between fluorescence anisotropy and true strain in polymer films*. 2024, figshare DOI: 10.6084/m9.figshare.27897528.
56. Luchowski, R., et al., *Fluorescence polarization standard for near infrared spectroscopy and microscopy.* Applied Optics, 2008. **47**(33): p. 6257-6265 DOI: 10.1364/AO.47.006257.
57. Haque, A., et al., *Type-II CdSe/ZnO Core/Shell Nanorods: Nanoheterostructures with A Tunable Dual Emission in Visible and Near-Infrared Spectral Ranges.* Advanced Functional Materials, 2024. **34**(16): p. 2305296 DOI: https://doi.org/10.1002/adfm.202305296.
58. Handique, K.C., Barman, B., and Kalita, P.K., *Effect of Zn2+ ion concentration on the optoelectronic properties of chemically synthesized ZnSe nanorods.* Physica B: Condensed Matter, 2024. **674**: p. 415571 DOI: https://doi.org/10.1016/j.physb.2023.415571.
59. Shin, D.J., et al., *Polarized emission from unidirectionally oriented semiconductor nanorods in light-emitting devices.* Applied Surface Science, 2023. **614**: p. 156160 DOI: https://doi.org/10.1016/j.apsusc.2022.156160.
60. Castelletto, S. and Boretti, A., *Luminescence solar concentrators: A technology update.* Nano Energy, 2023. **109**: p. 108269 DOI: https://doi.org/10.1016/j.nanoen.2023.108269.
61. Elzière, P., et al., *Supramolecular Structure for Large Strain Dissipation and Outstanding Impact Resistance in Polyvinylbutyral.* Macromolecules, 2019. **52**(20): p. 7821-7830 DOI: 10.1021/acs.macromol.9b01277.
62. Warner, T., et al., *Data for "Effect of luminescent nanocrystal alignment on fluorescence anisotropy and light guiding in polymer films"*. 2024, figshare DOI: 10.6084/m9.figshare.27901611.